

# The stellar mass content of distant galaxy groups

Michael L. Balogh<sup>1</sup>, Dave Wilman<sup>2</sup>, Robert D. E. Henderson<sup>1</sup>, Richard G. Bower<sup>3</sup>,  
David Gilbank<sup>4</sup>, Richard Whitaker<sup>3</sup>, Simon L. Morris<sup>3</sup>, George Hau<sup>3</sup>, J. S. Mulchaey<sup>5</sup>,  
A. Oemler Jr.<sup>5</sup> and R. G. Carlberg<sup>4</sup>

<sup>1</sup>Department of Physics and Astronomy, University of Waterloo, Waterloo, Ontario, N2L 3G1, Canada

<sup>2</sup>Max-Planck-Institut für extraterrestrische Physik, Giessenbachstrasse 85748 Garching Germany

<sup>3</sup>Department of Physics, University of Durham, Durham, UK, DH1 3LE

<sup>4</sup>Department of Astronomy and Astrophysics, University of Toronto, Toronto, Ontario, M5S 3H8, Canada

<sup>5</sup>Observatories of the Carnegie Institution of Washington, 813 Santa Barbara Street, Pasadena, California, USA

19 July 2018

## ABSTRACT

We have obtained near-infrared imaging of 58 galaxy groups, in the redshift range  $0.1 < z < 0.6$ , from the William Herschel Telescope and from the *Spitzer* IRAC data archive. The groups are selected from the CNOC2 redshift survey, with additional spectroscopy from the Baade telescope (Magellan). Our group samples are statistically complete to  $K_{\text{Vega}} = 17.7$  (INGRID) and  $[3.6\mu\text{m}]_{\text{AB}} = 19.9$  (IRAC). From these data we construct near-infrared luminosity functions, for groups in bins of velocity dispersion, up to  $800 \text{ km s}^{-1}$ , and redshift. The total amount of near-infrared luminosity per group is compared with the dynamical mass, estimated from the velocity dispersion, to compute the mass-to-light ratio,  $M_{200}/L_K$ . We find that the  $M_{200}/L_K$  values in these groups are in good agreement with those of their statistical descendants at  $z = 0$ , with no evidence for evolution beyond that expected for a passively evolving population. There is a trend of  $M_{200}/L_K$  with group mass, which increases from  $M_{200}/L_K \approx 10$  for groups with  $\sigma < 250 \text{ km s}^{-1}$  to  $M_{200}/L_K \approx 100$  for  $425 \text{ km s}^{-1} < \sigma < 800 \text{ km s}^{-1}$ . This trend is weaker, but still present, if we estimate the total mass from weak lensing measurements. In terms of stellar mass, stars make up  $\gtrsim 2$  per cent of the mass in the smallest groups, and  $\lesssim 1$  per cent in the most massive groups. We also use the near-infrared data to consider the correlations between stellar populations and stellar masses, for group and field galaxies at  $0.1 < z < 0.6$ . We find that fewer group galaxies show strong [OII] emission compared with field galaxies of the same stellar mass and at the same redshift. We conclude that most of the stellar mass in these groups was already in place by  $z \sim 0.4$ , with little environment-driven evolution to the present day.

**Key words:** galaxies: clusters, luminosity function, mass function, infrared:galaxies

## 1 INTRODUCTION

In hierarchical models of structure formation, small groups of galaxies represent an important environment that connects active, star-forming field galaxies to quiescent cluster galaxies. In this context they may be the environment in which the star formation histories of galaxies are dramatically altered. Since a large fraction of galaxies in the nearby Universe exist within groups (e.g. Huchra & Geller 1982; Eke et al. 2004a), such group-driven transformations could have a dominant influence on galaxy evolution, at least since  $z \sim 1$ . However, galaxy groups are not well understood relative to field galaxies and larger clusters, especially beyond the local universe. Their low-contrast relative to the background means that deep, highly complete redshift surveys are needed to compile

large enough samples of member galaxies, and to minimize the effects of selection biases.

Now that the global history of star formation over the past few billion years is well established (e.g. Heavens et al. 2004; Hopkins 2004; Juneau et al. 2005), the next important goal is to trace star formation and efficiency in different clustering environments (e.g. Balogh et al. 2004; Eke et al. 2004b; Cooper et al. 2006). An important integral quantity that traces this evolution is the relative amount of luminous matter in groups of different masses. Studies at optical wavelengths have shown that, locally at least, the ratio between dynamical mass and optical light ( $M_{200}/L_{\text{opt}}$ ) increases strongly with mass, up to systems with masses of a few times  $10^{13} M_{\odot}$ , typical of poor clusters (e.g. Girardi et al. 2002; Eke et al. 2004b). Semi-analytic models of galaxy formation with reasonable feedback schemes are in good agreement with this trend

(Eke et al. 2004b). Recently, Parker et al. (2005) have made measurements of  $M_{200}/L_{\text{opt}}$  in galaxy groups selected from the second Canadian Network for Observational Cosmology (CNOC2) field galaxy redshift survey (Carlberg et al. 2001), with masses determined by weak lensing (Hoekstra et al. 2001). They, too, find a trend of increasing  $M_{200}/L_{\text{opt}}$  that is consistent with that measured at lower redshift.

A difficulty in interpreting the above results is the sensitivity of optical luminosity to recent star formation, which has a strong environmental dependence (e.g. Balogh et al. 2004; Blanton et al. 2005; Baldry et al. 2006). Near-infrared (NIR) luminosities are superior in this respect, because they trace stellar mass, independent of star formation history, to within a factor of a few (e.g. Bell & de Jong 2001). A few near-infrared studies of nearby groups have been undertaken (Lin et al. 2004; Ramella et al. 2004), and these observations generally find an increase in  $M_{200}/L_K$  (the ratio between dynamical-mass and near-infrared light) with mass, comparable to that seen at optical wavelengths. However, until now such measurements have not yet been reported for more distant groups.

It is the purpose of this paper to measure  $M_{200}/L_K$  for groups at  $0.1 < z < 0.6$  for the first time, using both ground-based (K-band) and *Spitzer* ( $3.6\mu\text{m}$ ) imaging of 58 galaxy groups from the CNOC2 survey. The paper is outlined as follows: In §2 below we review the CNOC2 survey, discuss our observations, data reduction techniques and methods of group member selection. We present the luminosity functions and  $M_{200}/L_K$  as a function of group redshift and velocity dispersion in §3. The implications of these measurements, interpreted as stellar masses, are discussed in §4, and our conclusions are summarized in §5. Throughout this paper we assume a cosmology with matter density  $\Omega_m = 0.3$ , energy density  $\Omega_\Lambda = 0.7$ , and current Hubble constant  $H_0 = 100h \text{ km s}^{-1} \text{ Mpc}^{-1}$  with  $h = 0.75$ .

## 2 THE DATA

### 2.1 The redshift surveys

Our galaxy group sample is derived from the CNOC2 redshift survey, which was conducted at the Canada-France-Hawaii telescope using the multiobject spectrograph (MOS), with the primary goal of studying galaxy populations, clustering, and evolution (Yee et al. 2000). This spectroscopic and photometric survey consists of approximately 6000 galaxies with a measured redshift, distributed in four widely separated patches covering a total of  $\sim 1.5 \text{ deg}^2$  of the sky. Although the survey area is small relative to more recent redshift surveys, the use of four noncontiguous patches ensures that our group sample is not likely to be strongly biased due to cosmic variance. The survey includes  $U, B, V, R_c, I$  photometry, and the initial spectroscopic sample was selected from the  $R_c$  (hereafter just  $R$ ) images. The colours are k-corrected to the rest-frame using the template-fitting code of Blanton & Roweis (2006). Each MOS pointing was observed with two masks, to increase completeness in dense fields. There are redshifts for about 50 per cent of galaxies to  $R = 21.5$ ; this completeness is magnitude-dependent, as slits were primarily allocated to brighter galaxies.

Recently we re-observed 20 fields in three of the four patches with the LDSS2 spectrograph on Magellan (Wilman et al. 2005a). There were two main aims of this additional spectroscopy. The first was to cover each group with sufficient masks (between one and three) to achieve near-100 per cent completeness at bright magnitudes. This is important because measurements of quantities like

total stellar mass will be strongly affected by the brightest galaxies, and their small number per group will make statistical corrections unreliable on an individual group basis. Furthermore, the use of a larger telescope and better spectrograph allows us to obtain redshifts for fainter galaxies, and we obtain a good statistical sampling of galaxies as faint as  $R = 22$ . The main advantage for our present purposes is that this increases the number of members per group, allowing us to obtain better measurements of the group geometry and velocity dispersion.

From the CNOC2 and Magellan spectra we also measure the rest-frame equivalent width of the [OII] emission line,  $W_\circ([\text{OII}])$ , as an indicator of ongoing star formation. This line strength is measured following the definition of Balogh et al. (1997). In the fields covered by our LDSS2 spectroscopy, the line measurements are the same as those presented by Wilman et al. (2005a); for the rest of the CNOC2 sample, the measurements will be presented in a future paper (Whitaker & Morris, in preparation).

### 2.2 Galaxy Group Membership

Virialized galaxy groups within the CNOC2 patches were initially identified in redshift space by Carlberg et al. (2001) using an iterative friends-of-friends algorithm on the catalogued galaxies. Over 200 groups were found, with an average of 3.8 confirmed members per group. The search by Carlberg et al. (2001) limited the sample's  $k$ -corrected and evolution-compensated absolute luminosity to brighter than  $M_R^{ke} = -18.5 \text{ mag}$ . To take advantage of the increased depth and completeness afforded us by the Magellan data, in this paper we redefine the original group membership, in a manner similar to that described in Wilman et al. (2005a). To summarize briefly, an iterative procedure is implemented to select galaxies with redshifts within twice the group velocity dispersion and with a transverse distance from the group centre which is within 1/5 of the line-of-sight distance. In each iteration, the velocity dispersion is recomputed using the Gapper estimate (Beers et al. 1990), and the centre is recomputed as the luminosity-weighted geometric centre of the group members. This procedure is applied to the whole group sample, including those that were not re-observed with LDSS2, so that membership is consistently defined.

To compute the virial mass of all the galaxy groups we used a theoretical estimate based on the velocity dispersion,  $\sigma$ . Assuming that the groups are in dynamical equilibrium, the total mass contained within a volume of  $\frac{4}{3}\pi R_{200}^3$  is given by

$$\mathcal{M}_{200} = \frac{3}{G} R_{200} \sigma^2, \quad (1)$$

where the ‘‘virial radius’’  $R_{200}$  is

$$R_{200} = \frac{\sqrt{3}\sigma}{10H_0(1+z)^{1.5}}. \quad (2)$$

Although we are well aware that velocity dispersion is not a perfect indicator of mass, especially for these poor systems with few members, we keep this definition so that we can directly and easily compare our results with the literature (e.g. Ramella et al. 2004). In Section 4.1 we will consider how the use of available weak-lensing masses affects our results.

As described in the following sections, we have obtained near-infrared imaging for 58 groups, and these are the only groups we will consider in the remainder of this paper. The list of groups and their properties are given in Table 1, for those groups with only data from the original CNOC2 survey, and in Table 2 for those re-observed with Magellan. Included in the tables are the group coordinates, redshift, intrinsic velocity dispersion (i.e., accounting for

**Table 1.** Properties of galaxy groups from the original Carlberg et al. (2001) sample (i.e. not reobserved at Magellan) with good near-infrared coverage. Column 1 gives the group id from Carlberg et al. (2001), modulus factors of 100 added to distinguish groups in different patches. Columns 2-4 give the central position and redshift of the group. Column 5 is the estimated intrinsic velocity dispersion, and column 6 is the number of galaxies used to obtain this number. Columns 7 and 8 are the virial radius and mass calculated from the velocity dispersion. Entries marked with an \* are upper limits. The numbers in columns (9), (10) and (11) are the number of galaxies with redshifts, within  $R_{200}$  in the  $R$ -band, *Spitzer* and INGRID catalogues, respectively.

(1)	(2)	(3)	(4)	(5)	(6)	(7)	(8)	(9)	(10)	(11)
Group	$\alpha$	$\delta$	$z$	$\sigma$	$N_\sigma$	$R_{200}$	$\mathcal{M}_{200}$	$N_z$	$N_z$	$N_z$
	(J2000)	(J2000)		( $km\ s^{-1}$ )		(kpc)	( $10^{12} \mathcal{M}_\odot$ )	(R)	( <i>Spitzer</i> )	(INGRID)
1	222.4258728	9.050009727	0.1647	211 ± 95	8	388 ± 174	1.21 ± 1.63	5	5	4
9	222.2241516	8.945289612	0.2616	194 ± 61	8	316 ± 99	0.83 ± 0.78	4	3	3
11	222.2881775	8.830399513	0.2708	185 ± 46	12	298 ± 75	0.71 ± 0.54	4	4	0
13	222.3945923	8.905659676	0.2712	397 ± 68	11	640 ± 110	7.05 ± 3.62	4	4	0
15	222.1999817	8.963080406	0.3071	308 ± 219	4	476 ± 338	3.14 ± 6.71	3	2	3
16	222.5902405	9.103640556	0.3063	254 ± 64	5	392 ± 100	1.76 ± 1.34	4	4	0
17	222.097641	8.784229279	0.3086	395 ± 92	8	610 ± 141	6.66 ± 4.62	3	0	3
18	222.0555878	8.9292202	0.3234	261 ± 264	4	397 ± 401	1.89 ± 5.74	4	0	4
19	222.5530853	8.960080147	0.3248	330 ± 115	6	499 ± 174	3.79 ± 3.96	4	4	0
21	222.4801636	9.646129608	0.3483	204 ± 73	7	301 ± 107	0.87 ± 0.93	6	0	5
29	222.4464874	8.852370262	0.3736	309 ± 158	7	443 ± 227	2.95 ± 4.53	4	4	0
30	222.4998779	8.82020092	0.3938	335 ± 87	8	469 ± 122	3.67 ± 2.85	5	4	0
36	222.3757324	9.153150558	0.4701	265 ± 308	4	343 ± 399	1.68 ± 5.85	4	4	0
202	36.58484268	0.4656900167	0.1883	341 ± 288	5	607 ± 513	4.91 ± 12.45	4	4	0
206	36.37388992	0.2616599798	0.2284	261 ± 63	11	442 ± 106	2.09 ± 1.51	6	4	0
208	36.48381424	0.1982000023	0.2686	592 ± 165	8	956 ± 267	23.38 ± 19.54	7	7	0
217	36.44522095	0.3269200325	0.3082	696 ± 276	5	1074 ± 425	36.31 ± 43.12	5	5	0
221	36.52441406	0.07746999711	0.3578	73 ± 95	6	107 ± 139	0.04 ± 0.16	1	1	0
229	36.69626617	0.142960012	0.3833	540 ± 139	13	766 ± 197	15.56 ± 12.02	3	3	0
234	36.5413208	0.4848300517	0.3974	284 ± 111	7	397 ± 155	2.24 ± 2.62	3	3	0
239	36.36482239	0.2544400096	0.4083	608 ± 96	6	841 ± 133	21.72 ± 10.29	6	6	0
301	141.086853	36.9005127	0.1072	66 ± 86	6	130 ± 170	0.04 ± 0.15	2	2	0
302	140.2914429	36.71305847	0.112	123*	3	242*	0.26*	3	0	3
303	141.0169373	37.0852623	0.1913	331 ± 98	7	587 ± 175	4.48 ± 4	8	6	0
304	140.8880463	37.38243866	0.1914	121 ± 159	3	214 ± 282	0.22 ± 0.86	3	0	2
305	140.9043732	36.91950989	0.2025	243 ± 104	5	425 ± 182	1.75 ± 2.24	3	3	0
313	140.9319	37.01506042	0.2335	232 ± 97	7	391 ± 164	1.47 ± 1.85	4	4	0
315	141.0404053	36.99619293	0.2435	243 ± 45	13	404 ± 74	1.66 ± 0.92	5	5	0
317	140.9354401	37.34311676	0.2449	280 ± 66	12	465 ± 109	2.54 ± 1.79	9	0	6
329	140.9833832	37.25820923	0.3223	487 ± 79	4	739 ± 120	12.22 ± 5.94	1	0	1
333	140.8763885	37.14134979	0.3218	455 ± 143	9	692 ± 217	10.02 ± 9.42	6	5	4
336	140.8822021	36.8615303	0.3629	463 ± 531	4	672 ± 771	10.05 ± 34.58	4	4	4
337	140.9049683	37.7922287	0.3729	624 ± 184	7	895 ± 264	24.31 ± 21.54	6	0	4
344	141.0652008	36.88687134	0.3735	277 ± 77	12	397 ± 110	2.12 ± 1.77	3	3	0
346	141.004715	36.78276443	0.3733	393 ± 30	26	563 ± 44	6.06 ± 1.41	12	12	0
348	140.3150482	36.71141052	0.3789	82 ± 106	4	117 ± 151	0.05 ± 0.21	1	0	1
349	140.6838989	36.95294952	0.38	498 ± 108	8	710 ± 154	12.3 ± 8.02	3	0	3
350	140.5788269	36.81409073	0.3783	285 ± 85	7	407 ± 122	2.31 ± 2.08	3	0	3
351	140.965744	37.26145172	0.3795	143 ± 88	6	203 ± 126	0.29 ± 0.53	2	0	2
352	141.0719757	36.94703293	0.3791	386 ± 166	4	550 ± 236	5.72 ± 7.37	3	3	0
355	140.6422424	36.72232056	0.3907	349 ± 220	5	491 ± 310	4.18 ± 7.9	3	0	2
357	140.3446808	36.62179947	0.3909	133 ± 107	7	187 ± 151	0.23 ± 0.56	2	0	2
358	140.7977142	37.12773132	0.3908	287 ± 53	11	404 ± 75	2.32 ± 1.29	6	0	6
359	140.9085388	37.121418	0.3911	266 ± 127	4	375 ± 179	1.85 ± 2.65	3	3	3
361	140.7460632	36.83348846	0.4275	118 ± 156	3	159 ± 211	0.15 ± 0.61	2	0	2
365	141.1464691	37.03060913	0.473	122 ± 163	3	158 ± 211	0.16 ± 0.66	3	3	0
366	140.6099243	36.71389771	0.4728	455 ± 191	9	588 ± 246	8.49 ± 10.68	4	0	4

velocity uncertainties), virial mass, and the number of group members we identify within  $R_{200}$  above the  $R$ -completeness limit (see §2.3). The velocity dispersions were computed from all galaxies within  $1/h$  Mpc of the group centre (unless there were less than four members, in which case all galaxies were used); the number of galaxies contributing to the measurement of  $\sigma$  is given in the table as  $N_\sigma$ , as is the number of group members with either INGRID or *Spitzer* observations, as described in Sections 2.4 and 2.5.

### 2.3 Redshift completeness

The CNOC2 redshift survey is  $\sim 45$  per cent complete on average, with a dependence on  $R$  magnitude. For the original survey, Yee et al. (2000) computed statistical weights that correct for this incompleteness, and are valid to a limit of  $R = 21.5$ . The additional, Magellan spectroscopy we obtained (Wilman et al. 2005a) improves the depth around selected galaxy groups to  $R = 22$ . It

**Table 2.** As Table 1, but for the groups reobserved at Magellan (Wilman et al. 2005a), with good NIR data.

(1)	(2)	(3)	(4)	(5)	(6)	(7)	(8)	(9)	(10)	(11)
Group	$\alpha$ (J2000)	$\delta$ (J2000)	$z$	$\sigma$ ( $km\ s^{-1}$ )	$N_\sigma$	$R_{200}$ ( $kpc$ )	$\mathcal{M}_{200}$ ( $10^{12}\mathcal{M}_\odot$ )	$N_z$ (R)	$N_z$ ( <i>Spitzer</i> )	$N_z$ (INGRID)
23	222.3715668	9.511750221	0.3515	$510 \pm 113$	8	$749 \pm 167$	$13.58 \pm 9.06$	6	0	6
24	222.2642517	9.116889954	0.3592	121*	10	177*	0.18*	6	5	0
27	222.4210205	9.037179947	0.3725	$181 \pm 148$	3	$260 \pm 212$	$0.59 \pm 1.45$	3	2	3
28	222.5953522	9.018850327	0.3728	$161 \pm 79$	6	$231 \pm 113$	$0.42 \pm 0.61$	4	4	4
31	222.3106995	9.188610077	0.3929	$450 \pm 455$	4	$632 \pm 640$	$8.94 \pm 27.14$	3	2	0
32	222.4871063	8.929120064	0.3939	$591 \pm 120$	6	$829 \pm 169$	$20.22 \pm 12.32$	5	5	0
33	222.3906708	9.480049133	0.4066	$125 \pm 81$	6	$173 \pm 113$	$0.19 \pm 0.37$	2	0	2
37	222.3853607	9.073459625	0.4713	$236 \pm 79$	11	$305 \pm 102$	$1.18 \pm 1.19$	4	4	4
38	222.3486328	8.980949402	0.5106	$773 \pm 77$	14	$962 \pm 95$	$40.17 \pm 11.93$	10	8	0
39	222.3684692	9.496768951	0.5366	$461 \pm 104$	13	$559 \pm 126$	$8.29 \pm 5.59$	8	0	8
227	36.62685013	0.2123200148	0.3635	$341 \pm 144$	7	$495 \pm 209$	$4.02 \pm 5.08$	4	4	0

is difficult to combine the two samples in a statistically fair way; we thus keep them separate, and will refer to them as the R21.5 and R22 samples, respectively. These samples are exclusive: that is, galaxies and groups in the R22 sample are removed from the R21.5 sample, even though, of course, they formed part of the original CNOC2 survey. The statistical weights previously computed for both these surveys are magnitude- and position-dependent, but are computed from ensemble averages that may not appropriately account for any variation in completeness that depends on group richness, since groups with more members may be more incompletely sampled, despite the multiple-mask observing strategy. We have therefore recomputed the magnitude weights for group members as follows. First, the group sample is divided by velocity dispersion into those with  $\sigma < 200\ km\ s^{-1}$ ,  $200\ km\ s^{-1} < \sigma < 500\ km\ s^{-1}$  and  $\sigma > 500\ km\ s^{-1}$ . For each of these three subsamples, we compute the fraction of galaxies within  $R_{200}$  that have a redshift, as a function of  $R$  magnitude only, following the procedure described in Wilman et al. (2005a), but omitting the radial weight. For field galaxies, we use a simple magnitude-dependent weight that is computed independently for the R21.5 and R22 samples. Despite all these efforts, our results are only weakly dependent on the details of the weighting scheme. In particular, we find retrospectively that the incompleteness in the most massive groups is at most  $\sim 10$  per cent greater than the average. Magnitude weights are generally less than 1.5 for galaxies brighter than  $R=20$ , and increase up to a maximum of 5 (i.e. 20 per cent completeness) at  $R=22$ .

#### 2.4 K-band Observations and Data Reduction

Over the course of three nights during March 9-13, 2001, 25 fields centred on groups in the 9h and 14h CNOC2 patches were observed with the Isaac Newton Group Red Imaging Device (INGRID) on the 4.2m William Herschel Telescope (WHT). Each field was observed using a nine-point dither pattern with exposures of 10–15s in  $K_s$ . The total integration for each field varied, but was typically about 12 minutes. The data were reduced using the IPIPE NIR reduction pipeline (Gilbank et al. 2003). Briefly, this involved bad pixel-masking, flat fielding and sky-subtraction using a local flat field, and offset-finding and stacking of the sky-subtracted images to create a first-pass mosaic. An object mask was generated using SEXTRACTOR (Bertin & Arnouts 1996) to detect objects in this mosaic, and the sky-subtraction process was repeated after applying this mask to the individual exposures. This two step sky-subtraction technique avoids over-subtraction of the sky, as faint

objects undetected in a single frame can otherwise lead to an overestimate of the sky level. The second pass sky-subtracted frames were then combined into a final mosaic using a 3- $\sigma$  clipped mean.

Our magnitude zeropoints (on the Vega system) and astrometric solution were calibrated using the Two Micron All Sky Survey (2MASS; see Jarrett et al. 2000) point-source catalog  $K_s$ -band 4'' standard aperture magnitudes. Although the extended source catalog would have been a preferable source of photometry, there were not enough matching objects in our fields to obtain a reliable calibration. We used SEXTRACTOR v2.3.2 to obtain 4'' aperture magnitudes from our observations, and these were then compared to the matching 2MASS point-source catalog object magnitudes. For every field, the median of the differences between the SEXTRACTOR and 2MASS magnitudes was taken to be the zeropoint shift<sup>1</sup>.

For our analysis we adopt the MAG\_BEST photometry output from SEXTRACTOR. This gives a Kron (1980) magnitude if there is no danger of a nearby object biasing the magnitude measurement by more than 10 percent. If such crowding is an issue, a corrected isophotal magnitude is used instead. The perimeter of all images were trimmed such that most of the underexposed regions were not included in our analysis. We discarded all detected objects with SEXTRACTOR flags greater than 8. Two of the 25 images obtained were rejected entirely; one due to poor image quality, and the other due to poor seeing ( $\sim 1.7''$ ). Objects were then matched with the CNOC2 photometric catalogues (Yee et al. 2000). Unfortunately, the global astrometry of the optical catalogues is not better than  $\sim 5''$ . This effect was mitigated by adjusting the centroid of each field independently; over the relatively small INGRID field-of-view (4.1') the astrometry was good enough to allow reliable matching.

In the top panel of Figure 1, we show the K-R colour as a function of R magnitude, for all objects classified as galaxies. From the absence of blue galaxies fainter than  $R \sim 20$  we determine that the photometric magnitude limit is approximately  $K = 19.4$ . We will show below (§ 2.6) that this is much fainter than the completeness of the spectroscopic sample (shown as the dotted line), so all galaxies with redshifts are well-detected in the near-infrared.

<sup>1</sup> In practice this was done using the brightest sources, but fainter objects were included if there were enough of them to overcome the larger uncertainties on their individual magnitudes.

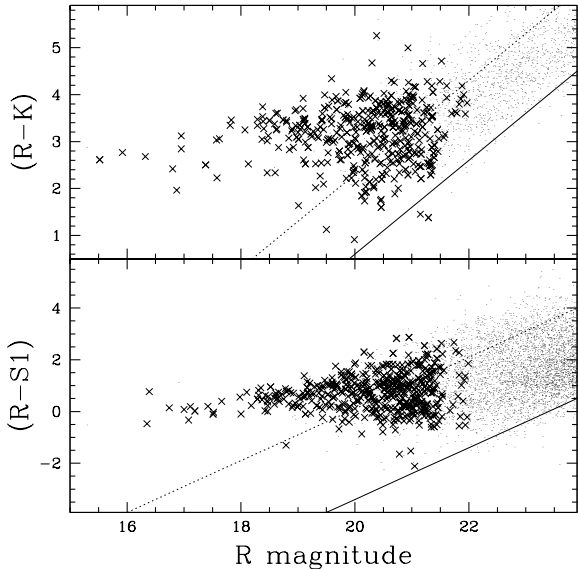


**Figure 1.** The optical-NIR colours of galaxies in the INGRID sample (top panel) and (for clarity) one-third of the *Spitzer* sample (bottom panel), as a function of  $R$  magnitude. Crosses represent galaxies with spectroscopic redshifts. The solid lines represent the photometric completeness of the IR data, which are  $K = 19.4$  and  $S1 = 23.4$ , respectively. The dotted lines represent the limits of  $K = 17.7$  and  $S1 = 19.9$  that correspond to the spectroscopic completeness limit for  $z < 0.6$  (see § 2.6).

## 2.5 Spitzer observations

Data taken with the *Spitzer* telescope Infrared Array Camera (IRAC) were obtained from the archive (GO program 64, PI G. Fazio). The pipeline-reduced images were used, and objects were detected in IRAC band 1 (AB magnitudes at  $3.6\mu\text{m}$ , hereafter denoted S1) with SEXTRACTOR v2.4.4. The detection criterion was a minimum of four pixels above a threshold of 1.5 times the global, rms background, with no filtering. The deblending algorithm used a minimum contrast of 0.00002, with 64 sub-thresholds. These parameters were chosen to optimize the deblending for matching with the optical catalogues. The object fluxes were determined from the improved MAG\_AUTO magnitude, which is recommended for the most recent versions of SEXTRACTOR.

Again, the relatively poor astrometry of the optical catalogues causes some difficulty in cross-correlation. For the 14h patch, we have improved the astrometric solution based on several *Hubble Space Telescope* pointings. However, in the 2h and 9h fields, the astrometric solution varies by  $\sim 5''$  across the overlapping IRAC field-of-view. Thus a larger matching radius was chosen ( $4''$  in the 2h field and  $5''$  in the 9h field), which causes an estimated  $\sim 10$  per cent of sources to be incorrectly matched. The photometric completeness is approximately  $S1=23.4$ , as shown in the bottom panel of Figure 1. As is the case with the K-band data, this is several magnitudes below our spectroscopic limit.

## 2.6 Completeness

We need to define the magnitude limits in both  $K$  and  $S1$  such that the spectroscopic sample of galaxies above these limits is statistically complete. This will be the case if  $R < 21.5$  (for the R21.5 sample) or  $R < 22$  (for the R22 sample) for all galaxies brighter than these limits. Figure 2 shows the optical-NIR colours as a func-

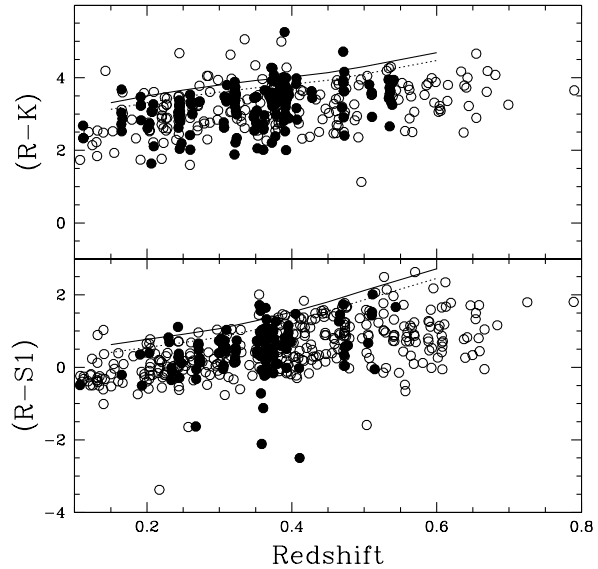


**Figure 2.** Observed optical-IR colours are shown as a function of redshift, for all galaxies with spectroscopic redshifts. Filled symbols represent group members. The  $R$  band magnitudes come from the CNOC2 catalogue, while the  $S1$  magnitudes (bottom panel) are from the *Spitzer* IRAC data, and the  $K$  magnitudes (top panel) are from INGRID. The lines are Bruzual & Charlot (2003) models for a solar metallicity, 13.7 Gyr model. The dotted line is dust-free, while the solid line includes  $\tau_v = 1$  magnitude of extinction, and thus provides a good estimate for the maximum possible colour for most normal galaxies.

tion of redshift, for the INGRID and *Spitzer* samples. The solid line shows a model of a solar metallicity, dust-reddened, 13.7 Gyr old stellar population from the Bruzual & Charlot (2003) models. Here and throughout the paper, we use the two-component dust model of Charlot & Fall (2000), assuming a visible optical depth to the youngest stars (with age  $< 10^7$  yr) of  $\tau_v = 1$ , and 30 per cent of this value toward older stars. The model provides a reasonable match to the red envelope of the data. The data and model indicate that, at  $z \leq 0.6$ , all normal galaxies should have  $(R - S1) \lesssim 2.1$  and  $(R - K) \lesssim 4.3$ . Galaxies redder than this (of which there are many in our photometric sample) are almost certainly at higher redshift. Given the  $R$ -completeness limits of the R21.5 and R22 samples, we therefore have the following NIR limits:

$$K_{\text{lim}} = \begin{cases} 17.2 & R21.5 \\ 17.7 & R22 \end{cases} \quad (3)$$

$$S1_{\text{lim}} = \begin{cases} 19.4 & R21.5 \\ 19.9 & R22 \end{cases} \quad (4)$$

In all cases, these magnitudes are well above the photometric completeness limits. Therefore, applying the weights appropriate to the R21.5 or R22 sample will provide statistically complete samples to these limits.

To compute the stellar luminosity of all group members, we need finally to account for the fact that some groups are only partially covered by *Spitzer* or INGRID imaging. For *Spitzer*, this generally occurs for groups that lie near the edge of the IRAC image. The INGRID images were centred on particular groups, but could still be incomplete if the virial radius (Equation 2) is larger than the field of view, or if there are background (or foreground) groups in

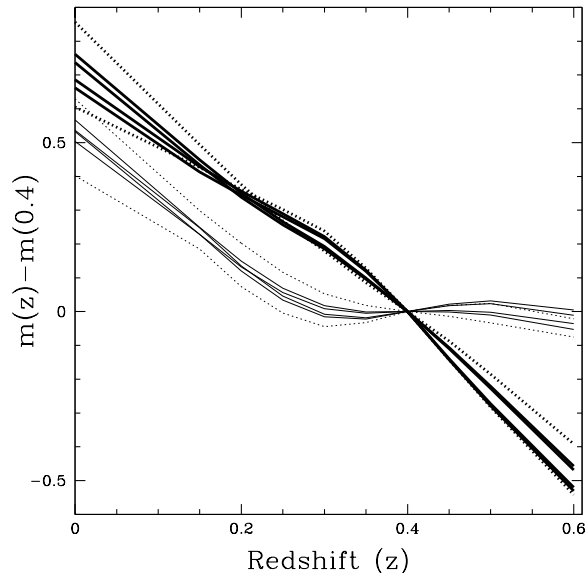


**Figure 3.** Model k-corrections, from a suite of Bruzual & Charlot (2003) models. The thick lines correspond to IRAC S1 AB magnitudes, while the thinner lines represent K (Vega) magnitudes. The solid lines, which are nearly indistinguishable from one another, represent solar metallicity models, with a Salpeter IMF. The four lines are all 13 Gyr models, with a) single stellar population (ssp), no dust; b) ssp,  $\tau_v = 1$  extinction; c) constant star formation rate (SFR), no dust; and d) constant SFR,  $\tau_v = 1$  extinction. The two models with dashed lines are constant SFR models, at supersolar and subsolar metallicity; these models provide the most different k-corrections. There is almost no sensitivity to population age or initial mass function (not shown).

the image that are not as well centred. For each group in the sample, therefore, we compute how many of the spectroscopic members have NIR data from either set of observations. Groups are only included in the sample if the fraction of members with NIR data is at least  $2/3$ , and for each group the members are weighted by the inverse of this fraction. These groups are listed in Table 1, with the number of spectroscopically confirmed group members with either INGRID or *Spitzer* observations. There are 29 (38) groups with good INGRID (IRAC) coverage, and a total of 58 that have coverage with at least one of the two instruments. When a galaxy is observed with both instruments, we use the IRAC data since it has the more stable zeropoint.

## 2.7 Combined infrared sample

To present luminosity functions it will be useful to have all the infrared data (taken in two different filters and over a range of redshifts) corrected to the same rest-frame wavelength range. We will take the approach, described in detail below, of converting the *Spitzer* S1 AB magnitudes to equivalent K-band (Vega) at  $z = 0.4$ , for ease of comparison to the literature. This magnitude will be denoted  $K_{\text{eq}}^{0.4}$  and is on the Vega system; note that  $K_{AB} \approx K_{\text{Vega}} + 2.0$ .

First, k-corrections are computed to convert the INGRID and IRAC magnitudes separately to the corresponding observed wavelength range at a fiducial redshift. To keep the correction as small as possible, where convenient we will show the data k-corrected to their typical group redshift of  $z = 0.4$ , rather than  $z = 0$ . To make these corrections we compute the difference in K magnitude rela-

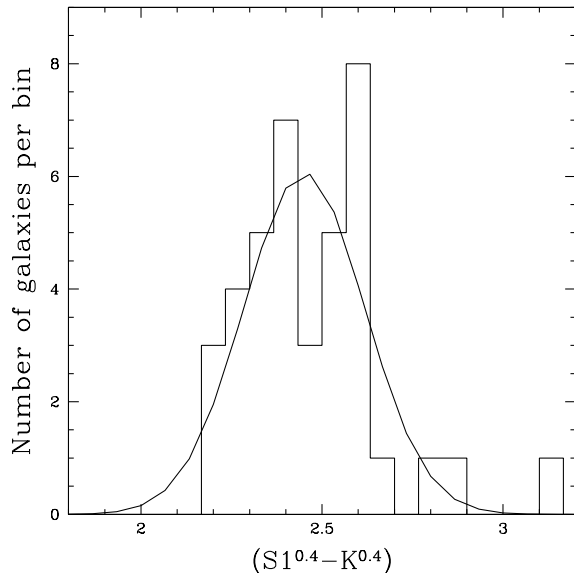


**Figure 4.** The distribution of  $(S1^{0.4} - K^{0.4})$  colours for the 39 galaxies observed with both INGRID and IRAC, and with  $0.3 < z < 0.6$ ,  $K < 17$  and  $S1 < 20$ . This colour is insensitive to the nature of the stellar population, so we use the mean colour (2.45) as a conversion between the two magnitudes. The solid line is a Gaussian with this mean, and standard deviation 0.17 mag, a best fit to the  $3\text{-}\sigma$  clipped data.

tive to  $z = 0.4$  for a variety of Bruzual & Charlot (2003) galaxy models. The results are shown in Figure 3, and the model parameters are described in the caption. Since the NIR fluxes are relatively insensitive to these parameters, the choice is not critical, and to a good approximation we find we can use

$$K(z) - K^{0.4} = \begin{cases} 0 & 0.3 \leq z < 0.6 \\ -1.73z + 0.52 & z < 0.3 \end{cases} \quad (5)$$

$$S1(z) - S1^{0.4} = \begin{cases} -2.50z + 1.0 & 0.4 \leq z < 0.6 \\ -1.8z + 0.72 & z < 0.4 \end{cases} \quad (6)$$

where  $K^{0.4}$  and  $S1^{0.4}$  refer to the observed band at  $z = 0.4$ .

After applying these corrections we can compare the  $K^{0.4}$  and  $S1^{0.4}$  magnitudes for galaxies observed with both instruments. In particular there are 39 such galaxies, with  $0.3 < z < 0.6$ ,  $K < 17$  and  $S1 < 20$  (one magnitude brighter than the photometric completeness limit, to reduce the impact of magnitude uncertainties). The distribution of  $(S1^{0.4} - K^{0.4})$  is shown for these galaxies in Figure 4. After clipping the only  $3\text{-}\sigma$  outlier, the mean and median are both 2.45, and the standard deviation is  $0.17 \text{ mag}^2$ . There is no significant trend of this difference with rest-frame optical colour or redshift. Thus we take the dispersion to represent the uncertainty in photometric calibration, including k-corrections and aperture effects. We convert our  $S1^{0.4}$  magnitudes to an equivalent  $K^{0.4}$  by

$$K_{\text{eq}}^{0.4} = S1^{0.4} - 2.45. \quad (7)$$

<sup>2</sup> We note that this colour is also in excellent agreement with predictions of the same models used to calculate the k-corrections: all models considered predict  $(S1^{0.4} - K^{0.4}) = 2.4 \pm 0.1$ .

**Table 3.** Average group properties, divided into redshift (column 1) and velocity dispersion ( $\sigma$ , column 2) bins. The other columns are: (3) The number of groups contributing to each bin; (4) the total observed, statistically weighted, rest-frame K-band luminosity within  $R_{200}$  and brighter than  $M^*$ ; (5) The total rest-frame K-band luminosity including a correction for galaxies below  $M^*$ , assuming  $\alpha = -0.8$ ; (6) the same as (5), but for  $\alpha = -1.09$ ; (7) the average dynamical mass in this bin; (8), the mass-to-light ratio, defined as column (7) divided by column (5).

(1) Redshift	(2) $\sigma$ (km s <sup>-1</sup> )	(3) $N_{groups}$	(4) $L_K, M_K < M_K^*$ (10 <sup>11</sup> $L_{K,\odot}$ )	(5) $L_{K,tot} (\alpha = -0.8)$ (10 <sup>11</sup> $L_{K,\odot}$ )	(6) $L_{K,tot} (\alpha = -1.09)$ (10 <sup>11</sup> $L_{K,\odot}$ )	(7) $M_{200}$ (10 <sup>13</sup> $M_\odot$ )	(8) $M_{200}/L_{K,tot}$ ( $M_\odot/L_{K,\odot}$ )
0.1–0.25	0–250	7	2.03 ± 0.4	4.48 ± 0.8	6.17 ± 1.1	1.06	23.77 ± 4.2
	250–425	4	3.08 ± 0.7	6.8 ± 1.6	9.36 ± 2.2	3.25	47.79 ± 11.4
0.25–0.37	0–250	5	4.23 ± 1.5	9.33 ± 3.4	12.85 ± 4.7	0.63	6.79 ± 2.5
	250–425	7	4.96 ± 1.5	10.94 ± 3.4	15.07 ± 4.6	4.04	36.91 ± 11.4
	425–700	7	3.41 ± 1.2	7.52 ± 2.6	10.36 ± 3.6	18.04	239.88 ± 84.4
0.37–0.6	0–250	9	2.97 ± 1	6.55 ± 2.3	9.02 ± 3.1	0.39	5.99 ± 2.1
	250–425	11	6.87 ± 0.8	15.17 ± 1.7	20.9 ± 2.3	3.64	24.01 ± 2.6
	425–800	9	9.19 ± 2.2	20.28 ± 4.9	27.93 ± 6.7	21.69	106.95 ± 25.8
0.1–0.6	0–250	21	2.95 ± 0.6	6.52 ± 1.4	8.98 ± 1.9	0.75	11.55 ± 2.5
	250–425	22	5.57 ± 1	12.3 ± 2.2	16.95 ± 3.1	3.67	29.81 ± 5.4
	425–800	15	7.1 ± 1.4	15.68 ± 3.2	21.59 ± 4.4	20.37	129.92 ± 26.4

Finally, from Equation 5 we see that the rest-frame K-band magnitudes are well approximated as

$$\begin{aligned} K_{rest} &= K^{0.4} + 0.52 \\ &= K_{eq}^{0.4} + 0.52. \end{aligned} \quad (8)$$

This k-correction between  $z = 0.4$  and  $z = 0$  is good to within about 0.05 mag, for all solar metallicity models considered.

### 3 RESULTS

#### 3.1 Luminosity Function

Most of our groups have less than about ten members with redshifts. To construct a luminosity function it is therefore necessary to stack the groups<sup>3</sup>. When computing the luminosity functions we consider only galaxies within  $R_{200}$ , which itself is estimated from the velocity dispersion of the group (Equation 2). Absolute magnitudes are computed from the  $K_{rest}$  magnitudes described above, according to our adopted cosmological model.

Since our data combine two spectroscopic samples, with different completeness limits, we first compute the luminosity function separately for the R21.5 and R22 samples, and then combine them, appropriately weighted according to the relative number of contributing galaxies. We have verified that the luminosity function for either sample alone is statistically consistent with that of the combined data. Since the R22 sample is more complete, this suggests that any systematic effects resulting from undersampling are masked by the larger, statistical uncertainties.

The luminosity function for all groups in the survey is shown in Figure 5. The number of galaxies per magnitude bin are weighted by the appropriate statistical weights, and divided by the number of groups contributing to that bin. The dotted line shows the luminosity corresponding to the magnitude limit of the highest redshift

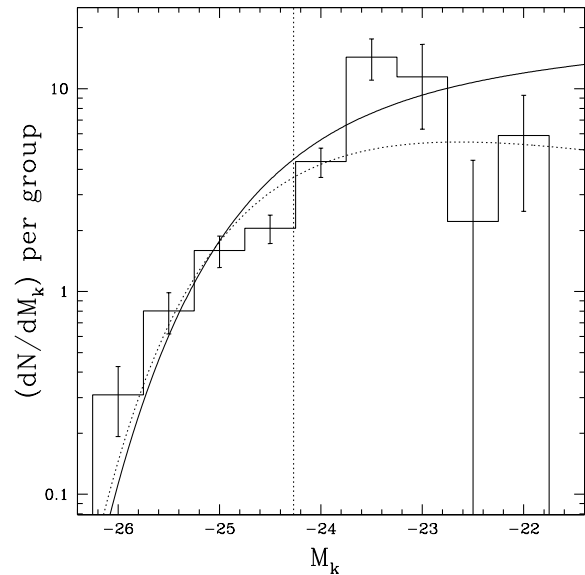


**Figure 5.** The luminosity function, per group, for all groups in the sample. The error bars are computed assuming Poisson statistics on the number of (unweighted) galaxies in each bin. The vertical, dotted line represents the brightest magnitude limit of all the groups in the sample; to the right of that line the data are still statistically complete, but there are progressively fewer contributing groups. The x-axis is the absolute rest-frame magnitude in the K filter. The curved, solid (dashed) line is a Schechter function with  $M_k^* = -24.38$  and  $\alpha = -1.09(-0.8)$ .

group in the sample; at fainter luminosities, fewer groups contribute to each bin.

We will not attempt to derive Schechter function parameters from our data, which are not much deeper than  $M^*$  and include few spectroscopic group members when the groups are binned by velocity dispersion (see below). However, it is necessary to assume some shape to correct the total group luminosity for galaxies below the magnitude limit. Drory et al. (2003) have measured the field K-band luminosity functions out to  $z = 1$ , and found

<sup>3</sup> As discussed in Section 2.3, the spectroscopic completeness is not a strong function of group size, which ensures that this stacked group is not dominated by sparsely-populated groups with large statistical weights; the weights are primarily a function only of apparent magnitude.

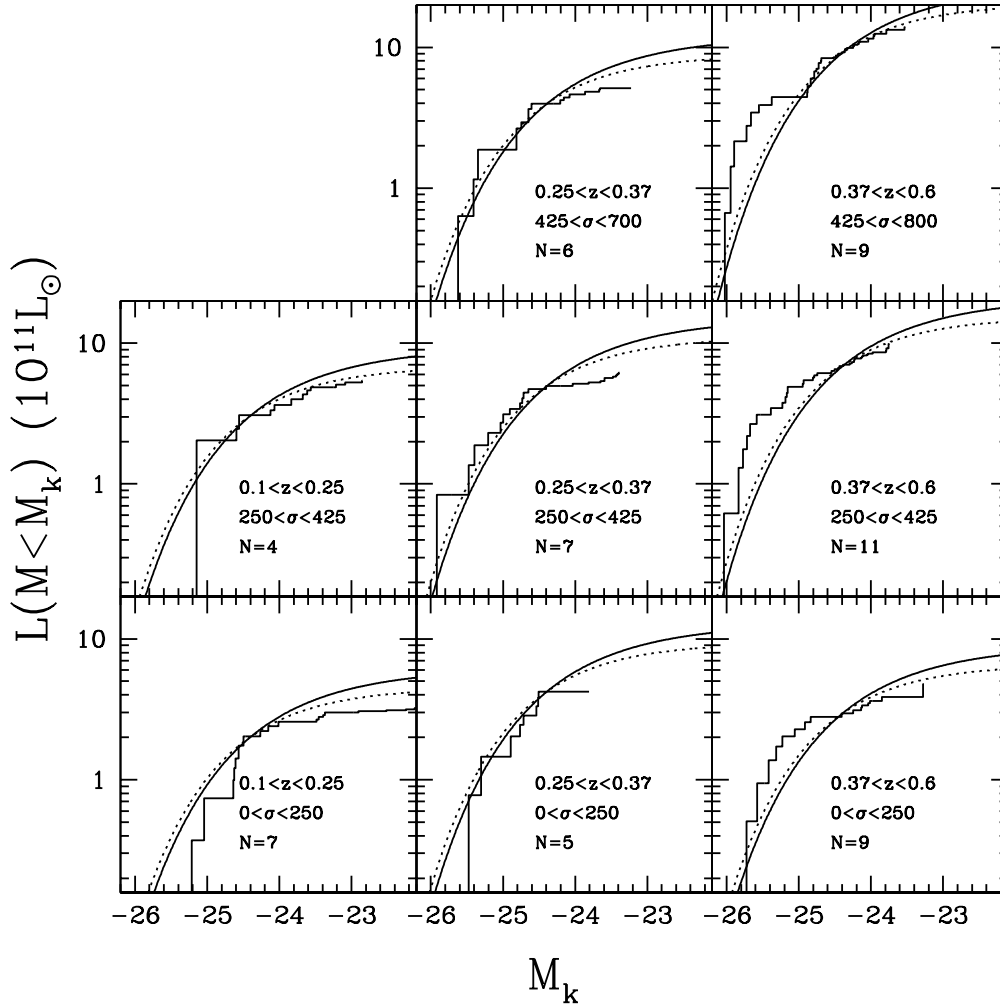


**Figure 6.** The cumulative luminosity per group, binned by group redshift and velocity dispersion as shown. Note that in this representation, the observational error bars (not shown) are not independent, and are largest at the brightest magnitudes. The number of groups contributing to each redshift and velocity dispersion bin is also shown in each panel. The x-axis is the rest-frame K-band absolute magnitude. The curved, solid (dotted) line is a Schechter function with  $M_k^* = -24.38$  and  $\alpha = -1.09(-0.8)$ . Both functions are normalized so that the total luminosity in galaxies brighter than  $M_k^*$  matches the observations.

(for  $h = 0.7$ )  $M_k^* = -24.16 - 0.53z$ ; at  $z = 0.4$ , therefore,  $M_k^* = -24.38$ . We will adopt this value throughout the paper, although we might expect  $M_k^*$  to vary by  $\sim 0.2$  mag over the full redshift range of our sample. Drory et al. (2003) cannot constrain the faint end slope, and so adopt  $\alpha = -1.09$  measured from 2MASS (Kochanek et al. 2001). However, the slope may be somewhat shallower in dense environments, more like  $\alpha = -0.8$  (e.g. Balogh et al. 2001; Ramella et al. 2004), so we will show both. The Schechter function using these parameters is shown in Figure 5, normalized to match the total luminosity of galaxies brighter than  $M_k^*$ ; both provide a reasonable description of the data, within the uncertainties.

### 3.2 Total group luminosities

In Figure 6 we show the *cumulative* luminosity distribution in groups, divided into redshift and group velocity dispersion bins. This alternative representation of the luminosity function shows the integrated K-band luminosity per group, brighter than a given mag-

nitude. Models are shown based on the Schechter functions presented in the previous section ( $M_k^* = -24.38$  and  $\alpha = -1.09$  or  $\alpha = -0.8$ ), always renormalized to match the total luminosity of all galaxies brighter than  $M_k^*$ . There is no dramatic change in the shape of the distribution with redshift or velocity dispersion, although an evolution of  $M_k^*$  of  $\sim 0.2$  mag over this redshift range, as found by Drory et al. (2003), would still be consistent with the data. For all bins, the data extend to  $M_k^*$  or deeper. To calculate the total luminosity, we will take the integral of the Schechter function fit; because of the way this is normalized, this is equivalent to adding up all the observed light brighter than  $M_k^*$  (including appropriate statistical weights), and using the Schechter function to extrapolate to zero luminosity. With this method of normalization the total luminosity is insensitive to the choice of  $M_k^*$ , and choosing a weakly evolving value would have no influence on our results. However, the integral does depend on the assumed value of  $\alpha$ , so we calculate results for both  $\alpha = -1.09$  and  $\alpha = -0.8$ . These results, as well as the total observed luminosity per group (uncorrected for the magnitude limit), are tabulated in Table 3.



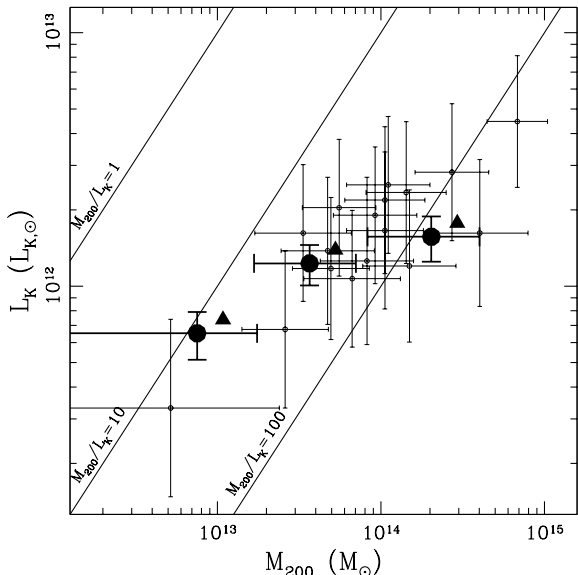


**Figure 7.** The total near-infrared luminosity of galaxy groups is shown as a function of dynamical mass, as estimated from the group velocity dispersion. The small, open symbols are low-redshift data from Ramella et al. (2004). The filled symbols are our groups, in three bins of velocity dispersion. The dynamical mass plotted is the weighted average mass of all groups in the bin. The error bars on this quantity show the minimum and maximum mass of the groups in this bin. The total stellar mass includes an extrapolation to zero luminosity, assuming  $\alpha = -0.8$ . The triangles include a small correction for passive evolution, based on a single stellar population model from Bruzual & Charlot (2003), and for hierarchical growth (in both the stellar and dark mass) from the Millennium simulation. The solid lines indicate lines of constant  $M_{200}/L_K$  ratio.

The uncertainty in the total luminosity assumes the unweighted number of galaxies per magnitude bin is described by a Poisson distribution. This accounts for the fact that most of the luminosity comes from the few brightest galaxies, which are generally the least numerous and therefore subject to the largest statistical fluctuation within a population of similar groups. It also accommodates the possibility that occasionally the brightest group galaxy may not have a spectroscopic redshift (as long as this galaxy isn't systematically overlooked in every group, and is not much brighter than the brightest galaxy for which we do have a redshift). Furthermore, the uncertainty scales with the statistical weight on the galaxy, so any incompleteness at the bright end of the luminosity function will be reflected in correspondingly larger error bars. In fact, our spectroscopic completeness is very high for the brightest galaxies, especially for the R22 sample, and therefore we are unlikely to have missed the brightest member galaxy in most groups.

### 3.3 Mass-to-light ratios

We are now in a position to compare the total NIR luminosity with the dynamical mass of the galaxy groups. The latter quantity is computed from the velocity dispersion (Equation 1) in the same way as Ramella et al. (2004), who performed a very similar experiment at  $z \approx 0$  (see below). The large, filled circles in Figure 7 represent our data, shown in three bins of velocity dispersion, but summed over all redshifts, as in the last three rows of Table 3. The filled triangles demonstrate the effect of applying two, relatively small, evolutionary corrections to our data. The first is an es-

timated correction for passive luminosity evolution, based on a single stellar population, dust-free Bruzual & Charlot (2003) model, that amounts to a  $\sim 30$  per cent reduction in luminosity, at fixed mass. The second correction aims to account for the hierarchical mass growth to  $z = 0$ . Using the results of the Millennium simulation (Springel et al. 2005), we find that haloes with  $M > 10^{13} M_{\odot}$  grow by  $\sim 43$  per cent between  $z = 0.4$  and  $z = 0$ , independent of initial mass. We assume that this growth occurs in both the luminosity and mass of the system, so the points move up and to the right, along lines of constant mass-to-light ratio. The net result of these two corrections is that the  $M_{200}/L_K$  of our  $z = 0.4$  groups are best compared to the  $M_{200}/L_K$  of  $z = 0$  systems that are  $\sim 40$  per cent more massive, as these represent, statistically, the most likely descendants.

The small, open symbols in Figure 7 represent the low-redshift data of Ramella et al. (2004). This is a sample of groups selected from a complete spectroscopic survey at  $z \approx 0$ , followed up with subsequent, deeper spectroscopy and cross-correlated with the 2MASS (Jarrett et al. 2000) to obtain near-infrared magnitudes. Thus the group selection is similar to ours, in that it is based on redshift-space clustering rather than X-ray or radio emission. There are naturally differences in our procedure for identifying groups and measuring their velocity dispersions, in part due to the fact that our galaxies are drawn from an incomplete redshift survey and, therefore, must be statistically weighted. However, due to the small number of members per group, our velocity dispersions are dominated by statistical uncertainties, rather than any systematic effects related to exactly which galaxies were included in the computation. For example, Wilman et al. (2005a) find that the deeper, more complete spectroscopic sampling from Magellan certainly improves the statistical uncertainties of our velocity dispersions, but does not reveal a systematic bias relative to measurements made from the original survey. Since we use the same equations to relate velocity dispersion to dynamical mass as Ramella et al. (2004), it is, therefore, possible to compare their data with ours to look for evolutionary trends.

There are two remarkable points about the result in Figure 7. The first is that our data lie within the scatter of the low-redshift data of Ramella et al. (2004). There has, therefore, been no strong evolution in the stellar mass fraction of galaxy groups since  $z = 0.4$ . Indeed, as is evident from the data in Table 3, we see no evidence for significant evolution within our sample itself, which spans the redshift range  $0.1 < z < 0.6$ . Given the statistical and systematic uncertainties we can rule out a pure luminosity evolution of a factor  $\sim 2$  or greater since  $z \sim 0.4$ . Also interesting is the suggestion that the  $M_{200}/L_K$  ratio at  $z = 0.4$  depends on system mass. The lowest mass groups in our sample have  $M_{200}/L_K \sim 10$ , while the most massive systems are a factor  $\sim 10$  larger. Again the large uncertainties preclude strong conclusions, but this is similar to the trend observed at low-redshift (Ramella et al. 2004; Lin et al. 2004). We will discuss this further in Section 4.

## 4 DISCUSSION

### 4.1 Lensing masses

Dynamical mass estimates based on velocity dispersion can be problematic for groups, both because of the small number of galaxies involved, and because of the difficulty of testing the necessary assumptions required to link velocity dispersion to mass. It is unclear, for example, how close these groups are to dynamical

**Table 4.** Similar to Table 3, but where we have included an estimate of the average lensing mass,  $\sigma_{\text{lens}}$ , in column (3), for each range of redshift-derived velocity dispersions (column 1). The lensing masses are derived from a fit between the lensing and dynamical velocity dispersion estimates in Parker (2005), and are used to calculate the cluster masses,  $R_{200}$ , and luminosity within  $R_{200}$ . Their uncertainties are the statistical uncertainties given in Parker (2005). The other columns are as in Table 3. The uncertainty in  $M_{200}/L_K$  (column 8) ignores any uncertainty in the mass, which would be correlated with the uncertainty in  $L_K$ .

(1)	(2)	(3)	(4)	(5)	(6)	(7)	(8)
Redshift	$\sigma_{\text{dyn}}$ ( $\text{km s}^{-1}$ )	$\langle\sigma_{\text{lens}}\rangle$ (estimated)	$L_K, M_K < M_K^*$ ( $10^{11} L_{K,\odot}$ )	$L_{K,\text{tot}} (\alpha = -0.8)$ ( $10^{11} L_{K,\odot}$ )	$L_{K,\text{tot}} (\alpha = -1.09)$ ( $10^{11} L_{K,\odot}$ )	$M_{200}$ ( $10^{13} M_\odot$ )	$M_{200}/L_{K,\text{tot}}$ ( $M_\odot/L_{K,\odot}$ )
0.1–0.6	0–250	$193 \pm 38$	$2.81 \pm 0.6$	$6.19 \pm 1.3$	$8.53 \pm 1.8$	0.88	$14.15 \pm 3$
	250–425	$270 \pm 39$	$5.57 \pm 1$	$12.3 \pm 2.2$	$16.95 \pm 3.1$	2.08	$16.93 \pm 3.1$
	425–800	$425 \pm 182$	$7.02 \pm 1.4$	$15.5 \pm 3.1$	$21.35 \pm 4.3$	6.53	$42.1 \pm 8.5$

equilibrium. Weak lensing provides a promising alternative, as this method measures the mass independently of the dynamical state of the group. Of course, this method has its own drawbacks, which are mainly the weakness of the signal, the sensitivity to choice of group centre, and the sensitivity to all mass projected along the line of sight between the observer and the lensed galaxy. Nonetheless, as the sources of systematic uncertainty are quite different from those associated with the velocity dispersions, they provide a useful check on our results.

Weak lensing masses have been measured for the CNOC2 group sample by Hoekstra et al. (2001) and Parker et al. (2005). However, due to the weakness of the lensing signal, this can only be done for ensembles, and Parker (2005) provide masses for three classes of groups, split by the velocity dispersion (as measured by Carlberg et al. 2001) at  $\sigma = 190 \text{ km s}^{-1}$  and  $\sigma = 500 \text{ km s}^{-1}$ . We make a linear fit to relate the lensing dispersions  $\sigma_{\text{lens}}$  (the velocity dispersion associated with an isothermal sphere of the measured mass) to the average dynamical values  $\sigma_{\text{dyn}}$ , and find<sup>4</sup>  $\sigma_{\text{lens}} = 113 \text{ km s}^{-1} + 0.49 \sigma_{\text{dyn}}$ . Using this fit as an estimate of the lensing mass for each individual group, we recompute  $R_{200}$  and  $M_{200}$  and repeat the entire analysis to measure the corresponding total NIR luminosity. This includes recomputing the NIR completeness of each group, since this depends on  $R_{200}$ , as well as the total luminosity within  $R_{200}$ . The results are shown in Table 4.

The main difference from the results in § 3.2 is that the masses of the groups with the highest velocity dispersion are lower than estimated using Equation 1. This leads to a lower value of  $M_{200}/L_K$  (despite the corresponding reduction in  $R_{200}$ ) and reduces the increase of  $M_{200}/L_K$  with system mass to a factor  $\sim 3$  between the lowest- and highest-mass groups in our sample.

## 4.2 Stellar mass-to-light ratios

While the near-infrared luminosities are closely related to stellar mass, there is still substantial variation in the stellar mass-to-light ratio ( $M_{\text{stellar}}/L_K$ ) with galaxy colour. We use the Bruzual & Charlot (2003) models to compute  $M_{\text{stellar}}/L_K$  as a function of galaxy colour, for a range of parameters. Assuming a Chabrier (2003) initial mass function, we model blue galaxies ( $B - V < 0.4$ ) as young galaxies with constant star formation and dust extinction of  $\tau_v = 1 \text{ mag}$ ; this gives  $M_{\text{stellar}}/L_K = 0.2$ . For red galaxies ( $B - V > 1$ ), a 11.7 Gyr old, dust-free single

<sup>4</sup> To be fully consistent, we use the original measurements of  $\sigma_{\text{dyn}}$  from Carlberg et al. (2001) to bin the groups in the same way as Parker et al. (2005), but then use our updated values to compute the average  $\sigma_{\text{dyn}}$  within each bin.

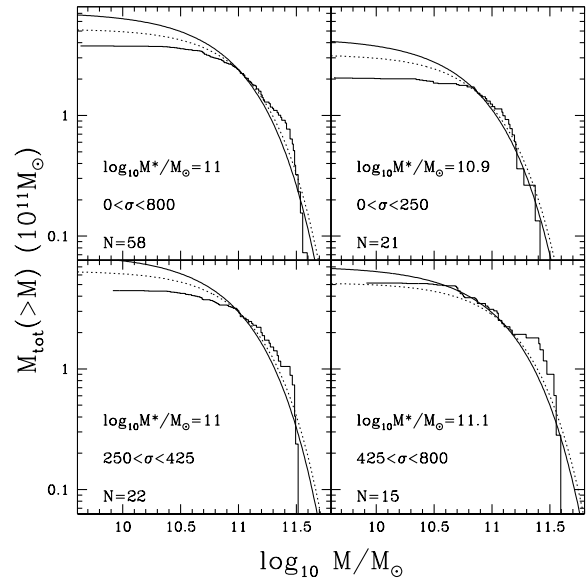


**Figure 8.** The cumulative stellar mass function for the whole group sample (top left panel) and for samples subdivided into bins of velocity dispersion (remaining panels, as labeled). The stellar masses are computed from the  $K_{rest}$  values, assuming the simple, colour-dependent  $M_{\text{stellar}}/L_K$  model described in the text. Each panel shows the number of groups contributing to each bin, and the value of  $M^*$  assumed for the Schechter functions, plotted as curved lines. The solid line assumes a faint end slope of  $\alpha = -1.09$ , while the dotted line assumes  $\alpha = -0.8$ . The Schechter functions are normalized to match the observed total stellar mass in galaxies with  $M > M^*$ .

stellar population model gives  $M_{\text{stellar}}/L_K = 0.7$ . For intermediate colours, we simply adopt a linear interpolation between these values.

The cumulative stellar mass functions are shown in Figure 8, for the whole group sample and for subsamples divided by velocity dispersion. The mass functions can be reasonably approximated by the Schechter functions shown, which have characteristic mass scales ranging from  $10^{10.9} M_\odot$  for the lowest-mass groups, and  $10^{11.1} M_\odot$  for the highest-mass groups. This trend for  $M^*$  to increase with density is well-known (e.g. Baldry et al. 2006). For the entire group sample, the ratio of dynamical mass to total stellar mass is  $168 \pm 25$ . In Figure 9 we show the dynamical-to-stellar mass ratio as a function of velocity dispersion, for both the  $\sigma$ -based and weak lensing-based mass (and  $R_{200}$ ) estimates. We also show the

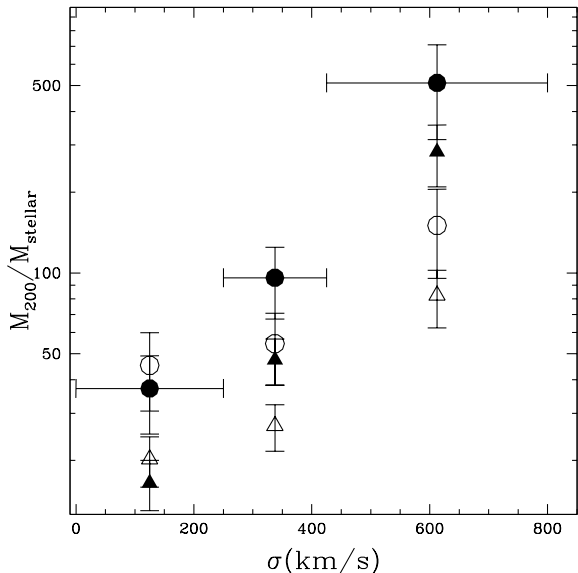


**Figure 9.** The dynamical-to-stellar mass ratio as a function of velocity dispersion. The solid points are computed assuming dynamical masses and  $R_{200}$  derived from the velocity distribution, while the open symbols use the weak-lensing derived masses. The circles are based on our simple colour-dependent  $M_{\text{stellar}}/L_K$  model, while the triangles assume  $M_{\text{stellar}}/L_K = 0.7$  for all galaxies. The three velocity dispersion bins are the same as in Figure 8, and the points are shown in the middle of each bin with the range indicated by the error bars on one set of points only, for clarity.

effect<sup>5</sup> of using a constant  $M_{\text{stellar}}/L_K = 0.7$ , as expected for early type galaxies, and typical of the Universal average at low redshift (e.g. Cole et al. 2001). The spread in the points at a given velocity dispersion therefore gives some indication of the systematic uncertainty on the measured  $M_{200}/M_{\text{stellar}}$ . As already noted, there is some discrepancy between the lensing-based and redshift-based results for the systems with the highest velocity dispersions, but overall the data show that  $M_{200}/M_{\text{stellar}}$  increases from  $\lesssim 50$  in the poorest systems to  $\gtrsim 100$  in the massive groups. This could be interpreted as a factor  $\sim 2$  difference in star formation efficiency between these haloes.

### 4.3 Colours and emission line strengths

In Wilman et al. (2005a), we found that the fraction of galaxies with [OII] emission increased with decreasing, rest-frame  $B_J$ -band luminosity, for both the group and field populations in the CNOC2 (R22) galaxy sample. We also found that, at fixed luminosity, emission line galaxies were more common in the field population. Using toy models (Wilman et al. 2005b) we claimed that this difference was due to a recent truncation of star formation in group galaxies, qualitatively similar to what is observed in more massive clusters at this redshift (e.g. Balogh et al. 1997, 2002; Nakata et al. 2005; Poggianti et al. 2006). However, that analysis was complicated by

<sup>5</sup> The difference between these two measurements is not simply related to the difference in average  $M_{\text{stellar}}/L_K$ , because the fixed value of  $M^*$  means the normalization of the Schechter function, and hence the extrapolation to  $L_k = 0$ , also differs in the two cases.

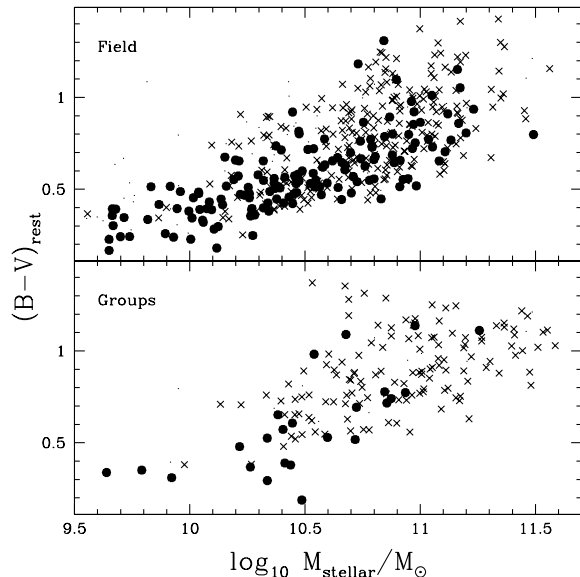


**Figure 10.** The correlation between  $(B-V)$  rest-frame colour and stellar mass, for the group (bottom panel) and field (top panel) samples. Both samples are restricted to the redshift range  $0.12 < z < 0.55$ , where there is no colour incompleteness. Only galaxies brighter than  $K = 17.2$  (corresponding to  $R = 21.5$ ) are shown (crosses), and group galaxies are restricted to those within  $R_{200}$ . Filled circles represent galaxies with strong emission lines,  $W_o([\text{OII}]) > 10\text{\AA}$ . The few small points represent galaxies for which no  $W_o([\text{OII}])$  measurement is available.

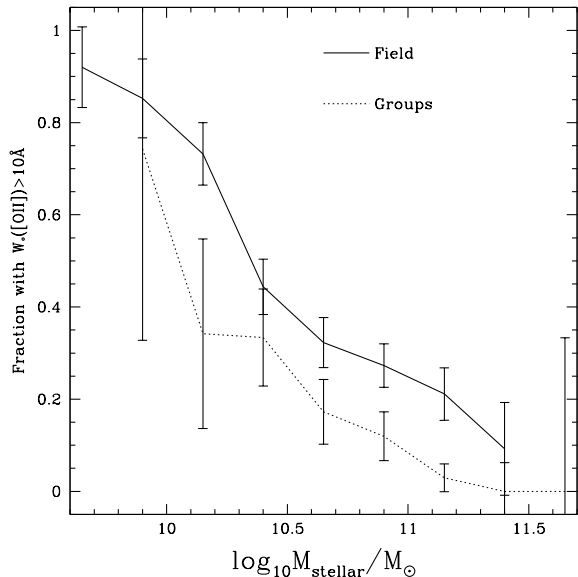
the fact that the rest-frame  $B_J$ -band luminosity is sensitive to recent star formation. Here we can re-examine the correlation as a function of stellar mass.

Figure 10 shows the rest-frame  $(B-V)$  colour as a function of stellar mass. We restrict the redshift range to  $0.12 < z < 0.55$ ; outside this range, colour-dependent incompleteness becomes important because few identifiable absorption features of red galaxies lie within the band-limiting filter used for the original CNOC2 spectroscopy (Yee et al. 2000). Within this range, all galaxies with redshifts are significantly detected in all filters, so there is no colour bias. Galaxies with strong emission lines ( $W_o([\text{OII}]) > 10\text{\AA}$ ) are shown as filled symbols.

Both the group and field populations exhibit a decrease in the fraction of blue, emission line galaxies as stellar mass increases. However, at fixed stellar mass, such late-type galaxies are less common in the group environment, compared with the field. This is illustrated more clearly in Figure 11, where we show the fraction of galaxies with strong emission lines ( $W_o([\text{OII}]) > 10\text{\AA}$ ) as a function of stellar mass, for the field and group samples. Thus we confirm our conclusions in Wilman et al. (2005b), that star formation in group environments was terminated earlier than in the lower-density field at  $z \sim 0.4$ .

### 4.4 Interpretation

The dominance of old stellar populations, together with the weakly-evolving mass-to-light ratio, implies that most of the stellar mass in groups must have already been in place by  $z \sim 0.4$ . Thus, we see no evidence of accelerated star formation in groups, despite the fact that the low velocity dispersions are expected to lead to enhanced dynamical interactions between group members. This is especially



**Figure 11.** The fraction of galaxies with strong [OII] emission lines is shown as a function of stellar mass, for the field and group sample at  $0.12 < z < 0.55$ . Error bars are  $1\text{-}\sigma$  jackknife resampling estimates.

surprising since our sample is at an epoch when the global star formation rate was several times higher than it is at present (e.g. Hopkins 2004). Unlike with group samples selected from their X-ray emission (e.g. Mulchaey et al. 2006), we have little reason to expect our redshift-selected sample to be biased toward especially relaxed or evolved groups, and therefore conclude that older stellar populations are characteristic of groups at  $z \sim 0.4$  in general.

Recent numerical simulations suggest that in overdense environments, dark matter haloes assembled their mass more rapidly, and at higher redshift, than haloes of the same mass in low-density environments (Gao et al. 2005), and this might be sufficient to explain the more evolved populations of galaxy groups and clusters without appealing to local interactions between galaxies and their environment (Maulbetsch et al. 2006). Determining whether or not this is a viable explanation for the observations presented here awaits a quantitative comparison with theoretical models.

## 5 CONCLUSIONS

We have presented near-infrared observations of 58 redshift-selected galaxy groups at  $0.1 < z < 0.6$ , obtained from the WHT and *Spitzer* space telescope. This affords us the first opportunity to obtain reliable stellar masses for galaxies in groups at this redshift. From these data we draw the following conclusions:

- There is evidence that the highest-mass groups in our sample ( $\sigma > 500 \text{ km s}^{-1}$ ) have  $M_{200}/L_K$  that are a factor  $\gtrsim 3$  larger than for the lowest-mass groups ( $\sigma < 200 \text{ km s}^{-1}$ ). This trend is present whether we use dynamically-estimated masses (from the velocity dispersions) or masses measured from a weak lensing analysis.
- Our best estimate of the group stellar mass fraction decreases from  $\sim 2$  per cent at  $\sigma < 200 \text{ km s}^{-1}$ , to  $\lesssim 1$  per cent in the most massive groups with  $\sigma > 500 \text{ km s}^{-1}$ .
- When comparing groups at  $z \sim 0.4$  to their statistically most-likely descendants at  $z = 0$ , we find no evidence for strong evo-

lution in  $M_{200}/L_K$  beyond that expected for a passively evolving population.

- Group galaxies have older stellar populations, as measured by their  $W_{\odot}([\text{OII}])$  emission or rest-frame (B-V) colour, than field galaxies of the same stellar mass.

We have demonstrated that galaxies in groups are predominantly old, passively evolving systems, even at  $z \sim 0.4$ . This is something of a surprise, given that effects such as tidal interactions and mergers (which are expected to induce star formation) should be more common, while more dramatic effects like ram-pressure stripping, often thought to play a role in terminating star formation within more massive clusters, should be negligible. Our results imply that these effects have not had a large influence on the properties of galaxies in groups since  $z \sim 0.4$ .

## 6 ACKNOWLEDGMENTS

We would like to thank the CNOC2 team for allowing us access to their unpublished data. We also gratefully acknowledge the efforts of the Virgo consortium, who have very usefully made the Millennium simulation results easily accessible, and we thank them specifically for allowing us access to the full simulation results prior to public release. M. Balogh would like to extend an especially warm thanks to Robert Greimel who completed the IN-GRID observations following a telescope scheduling change. This research was supported by the Natural Sciences and Engineering Research Council of Canada, through a Discovery Grant to M. Balogh, and an Undergraduate Research award to R. Henderson. D. Wilman is supported by a Max Planck Society Postdoctoral Fellowship. R. Henderson would like to thank the astronomy group at Waterloo, especially Gretchen Harris, for many helpful discussions.

## REFERENCES

- Baldry, I. K., Balogh, M. L., Bower, R. G., Budavari, T., Glazebrook, K. G., & Nichol, R. C. 2006, MNRAS, in press, astro-ph/0607648
- Balogh, M., Bower, R. G., et al. 2002, MNRAS, 337, 256
- Balogh, M. L., Christlein, D., Zabludoff, A. I., & Zaritsky, D. 2001, ApJ, 557, 117
- Balogh, M. L., Morris, S. L., Yee, H. K. C., Carlberg, R. G., & Ellingson, E. 1997, ApJL, 488, L75+
- Balogh, M. L. et al. 2004, MNRAS, 348, 1355
- Beers, T. C., Flynn, K., & Gebhardt, K. 1990, AJ, 100, 32
- Bell, E. F. & de Jong, R. S. 2001, ApJ, 550, 212
- Bertin, E. & Arnouts, S. 1996, A&AS, 117, 393
- Blanton, M. R., Eisenstein, D., Hogg, D. W., Schlegel, D. J., & Brinkmann, J. 2005, ApJ, 629, 143
- Blanton, M. R. & Roweis, S. 2006, AJ, submitted, astro-ph/0606170
- Bruzual, G. & Charlot, S. 2003, MNRAS, 344, 1000
- Carlberg, R. G., Yee, H. K. C., Morris, S. L., Lin, H., Hall, P. B., Patton, D. R., Sawicki, M., & Shepherd, C. W. 2001, ApJ, 552, 427
- Chabrier, G. 2003, PASP, 115, 763
- Charlot, S. & Fall, S. M. 2000, ApJ, 539, 718
- Cole, S., Norberg, P., Baugh, C. M., Frenk, C. S., et al. 2001, MNRAS, 326, 255
- Cooper, M. C. et al. 2006, MNRAS, 642

- Drory, N., Bender, R., Feulner, G., Hopp, U., Maraston, C., Snigula, J., & Hill, G. J. 2003, *ApJ*, 595, 698
- Eke, V. R. et al. 2004a, *MNRAS*, 348, 866
- . 2004b, *MNRAS*, 355, 769
- Gao, L., Springel, V., & White, S. D. M. 2005, *MNRAS*, 363, L66
- Gilbank, D. G., Smail, I., Ivison, R. J., & Packham, C. 2003, *MNRAS*, 346, 1125
- Girardi, M., Manzato, P., Mezzetti, M., Giuricin, G., & Limboz, F. . 2002, *ApJ*, 569, 720
- Heavens, A., Panter, B., Jimenez, R., & Dunlop, J. 2004, *Nature*, 428, 625
- Hoekstra, H. et al. 2001, *ApJL*, 548, L5
- Hopkins, A. M. 2004, *ApJ*, 615, 209
- Huchra, J. P. & Geller, M. J. 1982, *ApJ*, 257, 423
- Jarrett, T. H., Chester, T., Cutri, R., Schneider, S., Skrutskie, M., & Huchra, J. P. 2000, *AJ*, 119, 2498
- Juneau, S. et al. 2005, *ApJL*, 619, L135
- Kochanek, C. S., Pahre, M. A., Falco, E. E., Huchra, J. P., Mader, J., Jarrett, T. H., Chester, T., Cutri, R., & Schneider, S. E. 2001, *ApJ*, 560, 566
- Kron, R. G. 1980, *ApJS*, 43, 305
- Lin, Y., Mohr, J. J., & Stanford, S. A. 2004, *ApJ*, 610, 745
- Maulbetsch, C., Avila-Reese, V., Colin, P., Gottloeber, S., Khalatyan, A., & Steinmetz, M. 2006, *ApJ*, in press, astro-ph/0606360
- Mulchaey, J. S., Lubin, L. M., Fassnacht, C., Rosati, P., & Jeltema, T. E. 2006, *ApJ*, 646, 133
- Nakata, F., Bower, R. G., Balogh, M. L., & Wilman, D. J. 2005, *MNRAS*, 357, 679
- Parker, L. C. 2005, PhD thesis, University of Waterloo
- Parker, L. C., Hudson, M. J., Carlberg, R. G., & Hoekstra, H. 2005, *ApJ*, 634, 806
- Poggianti, B. et al. 2006, *ApJ*, 642, 188
- Ramella, M., Boschin, W., Geller, M. J., Mahdavi, A., & Rines, K. 2004, *AJ*, 128, 2022
- Springel, V. et al. 2005, *Nature*, 435, 629
- Wilman, D. J., Balogh, M. L., Bower, R. G., Mulchaey, J. S., Oemler, A., Carlberg, R. G., Morris, S. L., & Whitaker, R. J. 2005a, *MNRAS*, 358, 71
- Wilman, D. J. et al. 2005b, *MNRAS*, 358, 88
- Yee, H. K. C., Morris, S. L., Lin, H., Carlberg, R. G., Hall, P. B., Sawicki, M., Patton, D. R., Wirth, G. D., Ellingson, E., & Shepherd, C. W. 2000, *ApJS*, 129, 475